Case Studies in Chemical and Environmental Engineering 7 (2023) 100296

Contents lists available at ScienceDirect

Case Studies in Chemical and Environmental Engineering

journal homepage: www.sciencedirect.com/journal/case-studies-in-chemical-and-environmental-engineering

Case Report

Clean water recycling through adsorption via heterogeneous nanocomposites: Silver-based metal-organic framework embellished with graphene oxide and MXene

Mostafa Dadashi Firouzjaei [a,b,*], Ehsan Zolghadr [a,c], Ahmad Arabi Shamsabadi [d], Mohtada Sadrzadeh [b], Ahmad Rahimpour [b], Farhad Akbari Afkhami [e], Evan K. Wujcik [f], Mark Elliott [a,**]

[a] *Department of Civil, Construction, and Environmental Engineering, University of Alabama, Tuscaloosa, AL, 35487, USA*
[b] *Department of Mechanical Engineering, 10-367 Donadeo Innovation Center for Engineering, Advanced Water Research Lab (AWRL), University of Alberta, Edmonton, AB, T6G 1H9, Canada*
[c] *Department of Physics and Astronomy, University of Alabama, Tuscaloosa, AL, 35487, USA*
[d] *Department of Chemistry, University of Pennsylvania, Philadelphia, PA, 19104, USA*
[e] *Department of Chemistry, University of Alabama, Tuscaloosa, AL, 35487, USA*
[f] *Materials Engineering and Nanosensor [MEAN] Laboratory, Department of Chemical and Biomedical Engineering and the Advanced Structures & Composites Center [ASCC], The University of Maine, Orono, ME, 04469, USA*

ARTICLE INFO

Keywords:
MXene
Metal-organic frameworks (MOFs)
Water treatment
Dye adsorption
Nanocomposite materials
Graphene oxide

ABSTRACT

Cationic methylene blue (MB) and anionic orange G (OG) dyes were adsorbed using the first-ever synthesized nanocomposite of MXene-AgMOF. At 200 mg/L and 0.01 g, GO-AgMOF, MXene-AgMOF, and AgMOF were able to adsorb 99.9%, 99.0%, and 98.0% of cationic MB dye, respectively, from water. The nanocomposites were characterized both before and after adsorption using different characterization techniques. These nanocomposites show promise as cationic contaminant adsorbents, with an adsorption capacity of 399.9 mg/g for GO-AgMOF. Also, the enhanced adsorption capacity of AgMOF for anionic and cationic dyes suggests its potential use in environmental remediation when combined with MXene.

1. Introduction

The use of dyes in many chemical industries, such as plastics, paints, pulp and paper, and textiles, has been increasing in recent years. The release of dyes into water bodies raises serious environmental concerns as they are non-biodegradable, toxic, mutagenic, and carcinogenic [1]. Various methods have been adopted to remove dyes from wastewater, including nanofiltration [2,3], electrocatalysis [4], biological treatment [5], advanced oxidation [6], and adsorption [7]. Adsorption has been widely used to remove contaminants from wastewater due to its low energy consumption, simplicity, and cost-effectiveness [8,9]. Nevertheless, this method has some disadvantages, primarily low selectivity, adsorbent regeneration issues, and secondary waste generation [10,11]. To overcome these challenges, various materials, including metal oxides [12], MXenes [13], chitosan [14], carbon-based [15] nanostructures, and nanocomposites (NCs) have been studied for removing dyes.

Metal-organic frameworks (MOFs) have recently emerged as adsorbents [16–18] since these coordinated systems with metallic-organic structures can offer multiple reactive sites that are favorable to form hydrogen bonds [19–21], electrostatic interactions [22–24], acid-base interactions [25–27], and π-π interactions in aqueous media [28–30]. Some MOFs have shown low adsorption capacity due to low stability, insufficient pore volume, and surface area because the uncontrolled reaction between the organic ligand and metal salts can occur, leading to the formation of coarse and bulky structures with decreased active area for adsorption [31]. In order to overcome these issues, porous two-dimensional (2D) or three-dimensional (3D) materials have been incorporated during MOF fabrication to control their growth rate [32]. In this respect, hybrid materials were synthesized to achieve high adsorption sites [33–35] thereby increasing the surface area for

---

[*] Corresponding author. Department of Civil, Construction, and Environmental Engineering, University of Alabama, Tuscaloosa, AL, 35487, USA.
[**] Corresponding author.
E-mail addresses: mdfirouzjaei@crimson.ua.edu (M. Dadashi Firouzjaei), melliott@eng.ua.edu (M. Elliott).

https://doi.org/10.1016/j.cscee.2023.100296
Received 12 December 2022; Received in revised form 1 January 2023; Accepted 3 January 2023

improved dye adsorption [36,37]. The abundant oxygen-containing functional groups (hydroxyl groups on basal planes and carboxyl groups on the edges and epoxide) endow GO with a negative surface charge upon protonation, making it a promising additive to AgMOF for cationic dye removal [38,39]. MXenes, a new class of 2D material formed by the transition metal carbides, nitrides, or carbonitrides, can help increase the negative charge of the NCs to provide high adsorption sites for efficient cationic dye adsorption [13,40,41].

MXene's 2D structure is defined by n+1 layers of early transition metals (M), n layers of carbon or nitrogen (X), and surface terminations (T_x) like F, O, OH, or Cl. Topochemical selective etching of MAX phases produces MXenes [42]. MXene quality depends on MAX phases, hexagonal closed-packed layered carbides and nitrides (A in MAX refers to A-group elements of the periodic table, such as Al, Ga, and Si) [43]. Selective etching removes the A-layer atoms from the MAX phase, followed by delamination and exfoliating of loosely packed 2D MXene flakes. MXene could be made as a multilayered-powder or single-flake colloidal solution [43]. Colloidal MXenes are generated by exfoliating multilayered-MXenes to single-flake MXenes. MXene's large theoretical surface area, chemical stability, metallic conductivity, hydrophilicity, fine structure, and tuneable chemistry make it useful as an adsorbent for the removal of organic contaminants [44]. Besides MXene, graphene oxide (GO) nanosheets are another group of 2D materials composed of carbon atoms arranged in a honeycomb lattice; they have many hydroxyl, carboxyl, and epoxy functional groups [45]. Because of its high hydrophilicity, specific surface area, and reactive sites for chemical reactions, GO is an attractive component of nanocomposite structures [46]. Heterogeneous nanocomposites of GO, such as GO-MOF-based nanocomposites, are an attractive option for producing high-performance functional adsorbents [47].

In this study, a silver-based MOF (AgMOF) was functionalized by graphene-oxide (GO) and $Ti_3C_2T_x$ MXene to fabricate GO-AgMOF and MXene-AgMOF nanocomposites. While the synthesis of AgMOF and GO-AgMOF has been reported previously, MXene-AgMOF represents a novel nanocomposite with outstanding potential for dye adsorption. These NCs were characterized by X-ray diffraction (XRD), Raman spectroscopy, Fourier-transform infrared spectroscopy (FTIR), scanning electron microscopy (SEM) and transmission electron microscopy (TEM) to confirm successful fabrication. This work aims to investigate the effect of AgMOF composition with GO and MXene on water recycling and adsorption capacity. Methylene blue (MB) as a cationic dye and orange G (OG) as an anionic dye were used for adsorption experiments.

2. Methods

Materials. The following reagents were purchased from US VWR (Radnor, PA, US): methylene blue (MB) ($C_{16}H_{18}ClN_3S.H_20$); −1, 3, 5-benzentricarboxylic acid (BTC); silver nitrate ($AgNO_3$); ethanol (Purity, 99%). Graphene-oxide (GO) nanopowders (US1022) with 0.43–1.23 nm thickness and 1.5–5.5 μm diameter were purchased from US Research NPs, Inc. (Houston, USA).

Preparation of $Ti_3C_2T_x$ MXene. $Ti_3C_2T_x$ MXene sheets were prepared based on the method described earlier [48]. In brief, at ambient temperature, 1 g of LiF was dissolved in 20 mL of HCl (9 M) for 5 min. In the next step, 1 g of Ti_3AlC_2 was mixed in the solution, stirring under 500 rpm at 35 °C for 24 hours. A volume of 50 mL of deionized (DI) water was added to this mixture, which was then centrifuged at 3500 rpm speed for 5 min. The washing step was repeated 6 times until the final sediment was filtered and dried at room temperature to obtain the $Ti_3C_2T_x$ MXene flakes. The powder was then dispersed in water and sealed under a nitrogen atmosphere.

NCs Preparation and Synthesis. Fig. 1 shows the schematic of the fabrication process and characterization of NCs. To synthesize GO-AgMOF, first, 0.5 g of BTC was dissolved in 20 mL of ethanol and 0.5 g of silver nitrate was dissolved in 20 mL of water. The two solutions were mixed and 50 mg of GO powder was added to the mixture, which was then sonicated for 1 h using an ultrasonic probe at 0.5 pulses, 40 W output energy, and 20 kHz frequency (QSonica, Newtown, Connecticut, USA). The solution was then dried in the oven for 24 h at 40 °C. The same procedure was adopted for the fabrication of MXene-AgMOF, except that MXene powder was used in place of GO. For synthesizing AgMOF, an identical process was carried out, but without the addition of GO or MXene in the solution.

Characterization Techniques. The X-ray powder diffraction (XRD) data was obtained by Cu K_α radiation (Bruker D8, Billerica, USA) at 298 K at theta-2 mode from 5° to 60°. The Brunauer–Emmett–Teller (BET) process was performed to quantify the available surface area and the pore volume of the materials with an Autosorb iQ instrument

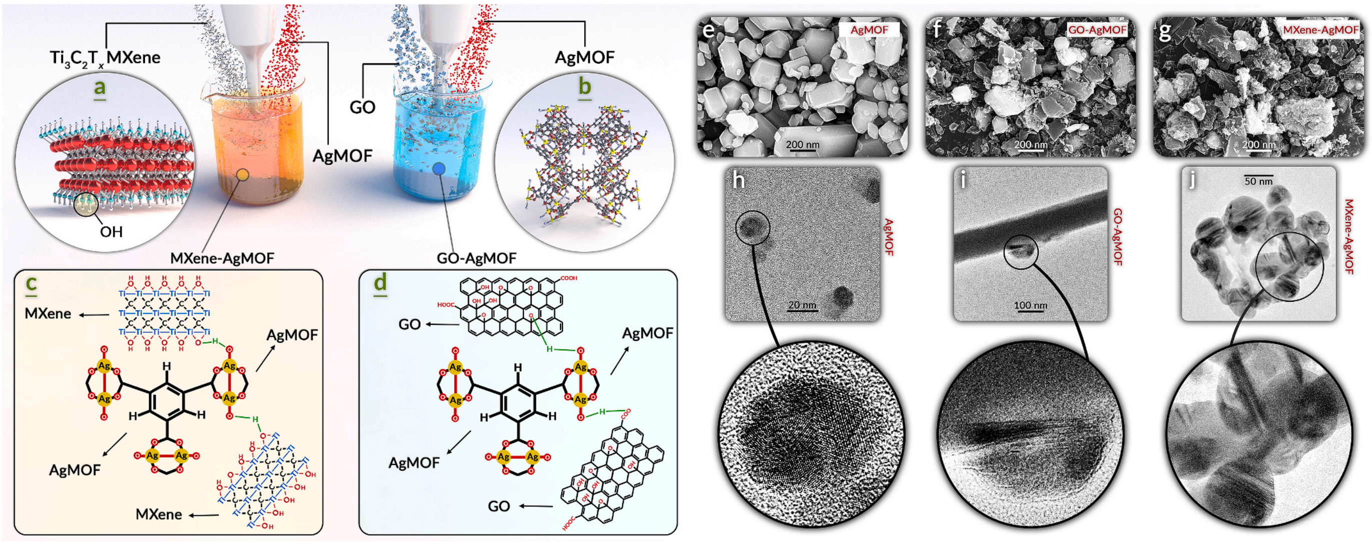

Fig. 1. Schematic illustration of NPs fabrication and chemical structure, as well as SEM and TEM representative micrographs. (a) 3D structure of $Ti_3C_2T_x$ MXene. (c) Chemical structure of MXene-AgMOF. MXene sheets are highly hydrophilic, and their hydroxyl groups facilitate hydrogen bonding to the other oxygen-containing groups of the AgMOF. (d) Chemical structure of GO-AgMOF. GO has many hydroxyl, epoxide, and carboxyl groups that are prone to share hydrogen with AgMOF. (e) SEM image of AgMOF. (f) SEM image of GO-AgMOF, showing that GO sheets and AgMOF crystals are strongly bonded. It should be noted that all of the NCs have been washed (centrifuged) and dispersed (ultrasonicated) in ethanol multiple times before the imaging. (g) SEM image of MXene-AgMOF, showing the composition of MXene and AgMOF. (h) TEM image of AgMOF. (i) TEM image of GO-AgMOF. (j) Bright-field TEM image of MXene-AgMOF.

(Quantachrome, USA). NANOTRAC WAVE II (Microtrac, Osaka, Japan) was used to determine the zeta potential of the nanoparticles (aqueous 0.5 M KCl) [49]. To obtain the MB and OG concentrations, UV–visible spectroscopy (UV–Vis) was applied at 665 nm and 491 nm wavelength, respectively (Genesys 10s, Thermo Fisher, USA).

The NCs surface morphology was investigated by scanning electron microscopy (SEM, Apreo Field Emission SEM, Thermofisher, USA) of gold-coated samples. Energy-dispersive X-ray spectroscopy (EDS) was utilized for mapping and elemental tracing of the synthesized NCs. Transmission electron microscopy experiments (TEM, FEI Tecnai F-20, Thermo Fisher, Waltham, USA) were performed for structural analysis. Also, Raman spectroscopy of NCs and loaded samples was carried out using a JASCO NRS-5500 Raman Spectrometer with a 532 nm laser.

Absorption Procedure. The adsorption capacity of the various materials was determined at room temperature at various initial dye concentrations (0–200 mg/L, pH = 7) by dispersing 0.01 g of adsorbents in 20 mL of aqueous dye solution. All the vials were shaken for 24 h at 150 rpm before measuring the residual dye in the solution and calculating the adsorbed amount. To investigate the effect of pH, 20 mL of the dye solutions with a concentration of 200 mg/L were prepared at various pH values; 0.01 g of adsorbent was then added to the dye-containing flasks) The pH was adjusted using 0.1 M NaOH and 0.1 M HCl. Triplicate samples of each condition previously mentioned were prepared and analyzed; the mean value is reported. The dye concentrations were determined by UV–Vis spectrophotometry and using an absorbance-concentration calibration curve. The adsorption removal efficiency, RE, and the adsorbent capacity, q, were calculated with Eqs (1) and (2):

$$RE(\%) = \left(\frac{C_0 - C_f}{C_0}\right) \times 100 \tag{1}$$

$$q = \frac{(C_0 - C_f)}{m} \times V \tag{2}$$

where V (L) is the volume of the dye solution, C_f (mg/L) is the final concentration of the dye, C_0 (mg/L) is the initial concentration, and m is the adsorbent mass added into the solution.

The adsorption data were calculated using Freundlich, Langmuir, and Temkin models using Eqs., (3), (4), and (5), respectively, as follows:

$$q_e = \frac{q_m \times k_L \times C_e}{1 + k_L \times C_e} \tag{3}$$

$$q_e = k_F \times {C_e}^{1/n} \tag{4}$$

$$q_e = B \times \ln k_T + B \times \ln C_e \tag{5}$$

The kinetics of adsorption were analyzed using pseudo-first-order, pseudo-second-order, and intra-particle diffusion models; see, respectively, **Eqs.**, **6**, **7**, and **8**:

$$\ln\left(q_f - q_t\right) = \ln q_f + k_1 t \tag{6}$$

$$\frac{1}{q_t} = \frac{1}{q_f} + \frac{1}{k^2 q_f^2} \times \frac{1}{t} \tag{7}$$

$$q_t = k_{id} t^{0.5} + C \tag{8}$$

In the above equations, q_t and q_f stand for the adsorption capacity at time t (h) and the end of the test, respectively, k_1 (1/min) is the rate constant of pseudo-first-order adsorption, k_2 (1/min) is the rate constant of pseudo-second-order adsorption, k_{id} (1/min) is the rate constant of the Temkin model and C is its intercept.

3. Results & discussion

Characteristics of Functionalized AgMOF. Fig. 1 summarizes the 3D and chemical structure of the materials. SEM and TEM images of the AgMOF and GO-AgMOF imply a typical crystalline and sheet-like structure that is consistent with our previous study [50]. While the former materials were thoroughly characterized by previous literature, this report focuses on the properties of new MXene-AgMOF, which were corroborated by a combination of techniques, with results summarized in Fig. S1. Specifically, Fig. S1a reports the characteristic Kα and Kβ peaks of titanium, respectively, at energies of 4.51 keV and 4.93 keV [51,52], indicating the presence of titanium in the survey area of the fabricated nanocomposite. Similarly, EDS analysis showed corresponding titanium and silver peaks [53]. The FTIR spectrum in Fig. S1b shows two sharp peaks at 2907 and 1062 cm^{-1} that are respectively assigned to the C–H and C–O stretching vibrations [54]. The peak at 1647 cm^{-1} is associated with the interaction of silver atoms with MXene nanosheets [55]. Moreover, the Ti–O stretching vibration is observed at around 575 cm^{-1} [54]. Fig. S1c presents the Raman spectrum of MXene-AgMOF. The two dominant peaks at ~1553 and ~1349 cm^{-1} are related to the aromatic benzene ring present in the AgMOF ligand. Indicative bonds of $Ti_3C_2T_x$ ($T_x = O_2$, OH) MXene are commonly reported at 210, 630, and 730 cm^{-1} [56,57]. Here, these peaks were detected approximately at 205, 620, and 711 cm^{-1}, i.e., slightly shifted, most likely due to the interaction with the AgMOF ligand. The Raman peaks at 205 and 711 cm^{-1} are respectively associated with the Ti–C and C–C vibrations of our oxygen-terminated MXene $Ti_3C_2O_2$, known as A_{1g} symmetry vibrations [58]. Finally, the peak at 620 cm^{-1} is usually related to the C atoms vibrations (known as Eg vibrations) in the OH-terminated MXene [58], which was not used in our experiment. A likely explanation is that the interaction of MXene and AgMOF ligand could replace one oxygen atom with a hydrogen atom, turning some oxygen-terminated MXene into an OH-terminated MXene structure. Furthermore, Fig. S1d presents XRD results of MXene-AgMOF in which the peaks observed at roughly 17.05° and 27.34° can be attributed to the diffractions of (004) and (006) planes in MXene [59,60].

Charge and Porosity of the NCs. The surface charge of the three materials fabricated in this study was evaluated by zeta potential measurements, where all the NCs showed a negative zeta potential (Fig. 2a). The GO-AgMOF and MXene-AgMOF demonstrated a lower pK than AgMOF. Various oxygen-containing functional groups on both GO and MXene appeared to increase the active charges at a slightly acidic pH [61–63]. The internal porosity and the availability of sites for adsorption of the various NCs were also evaluated with Brunauer, Emmett, and Teller (BET) tests by adsorption/desorption of nitrogen gas (Fig. 2b and c), with results summarized in Table 1. The numbers suggest that the BET surface area increased for both GO-AgMOF and MXene-AgMOF compared to traditional AgMOFs, with the GO-AgMOF nanocomposites associated with the largest surface area and pore volume. In particular, the surface area of GO-AgMOF was more than three times higher than that of AgMOF and nearly twice that of MXene-AgMOF.

3.1. Dye adsorption performance

Dye removal efficiency. GO-AgMOF achieved a specific mass adsorption of around 399.9 mg/g, allowing it to remove 99.9% of MB from solutions with a rather high starting dye concentration (200 ppm, Fig. 3) [66]. Also, AgMOF and MXene-AgMOF provided very high removal efficiency approaching 98% under similar conditions. Photographs of the experimental vials suggest that all the NCs formed floccules during MB adsorption, which is a crucial step for the secondary removal process and the separation of spent adsorbent from clean water in the case that the adsorbent is added as a powder. While NCs showed a promising adsorption capacity for MB, lower efficiency was observed with OG, implying that electrostatic interactions govern the adsorption phenomenon while not being the only forces at play. Although MXene-AgMOF improved the adsorption capacity of AgMOF towards OG, the observed efficiencies were consistently lower than 20% for OG, with q_e values of approximately 58 mg/g or lower.

The effect of pH on removal efficiency is summarized in Fig. 4. The

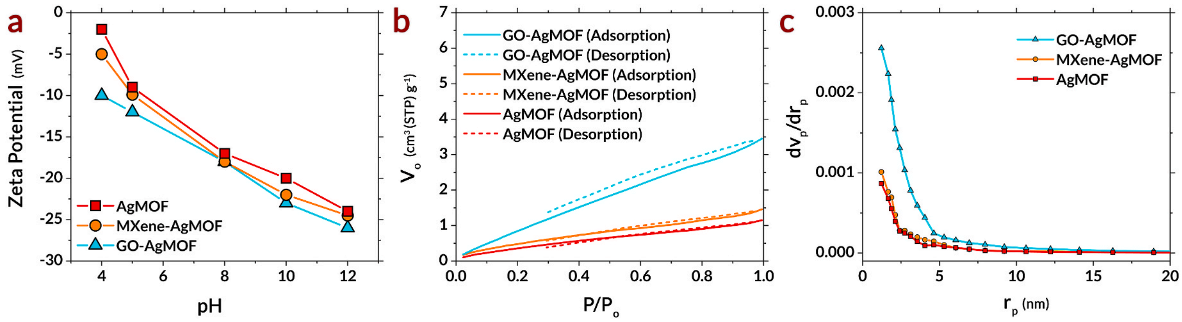

Fig. 2. **(a)** Zeta potential of the three NCs. **(b)** BET test results for nitrogen adsorption/desorption isotherms. GO-AgMOF is the only sample that showed a hysteresis, which demonstrates a typeIII isotherm. TypeIII isotherm occurs when the sample possesses a mesoporous structure, which translates into higher pore volume and surface area for the GO-AgMOF compared to the other two materials [64]. **(c)** Pore size distribution curve of the AgMOF, GO-AgMOF, and MXene-AgMOF, suggesting that all samples possessed a uniform pore size distribution [65].

Table 1
Physical characteristics of AgMOF, GO-AgMOF, and MXene-AgMOF.

Adsorbent	BET Surface Area (m^2/g)	Pore Volume (cm^3/g)	Mean Pore Diameter (nm)
AgMOF	1.3	0.001	5.6
GO-AgMOF	4.2	0.005	5.1
MXene-AgMOF	2.2	0.003	3.9

results suggest that the removal efficiency decreased with increasing pH for both dyes. At the alkaline range, deprotonation of MB solution can reduce the electrostatic attraction for adsorption onto the negatively charged adsorbents [66]. A similar trend was observed for OG, where the increased density of negative charges of the adsorbents at higher pH values repelled them for the surface, corroborating the dominant role of electrostatic interactions to drive adsorption.

Adsorption kinetics. The effect of contact time on the adsorption of MB and OG is displayed in Fig. 5 and suggests that for MB, >98% of adsorption efficiency (equal to a specific mass adsorbed >390 mg/g) was achieved after 14 h of exposure to the NCs. In the case of OG, after 14 h of the experiment, adsorption nearly stopped with specific mass adsorbed lower than 60 mg/g (15% adsorption efficiency). In order to further investigate the adsorption kinetics of AgMOF, GO-AgMOF, and MXene-AgMOF, experimental data in Fig. 5 were analyzed using the intra-particle diffusion, pseudo-first-order, and pseudo-second-order equations and the fitted parameters are displayed in Table 2. The pseudo-first-order model showed the best fit and the highest coefficient of determination (R-squared), while the pseudo-second-order did not adequately describe the adsorption data. The predicted specific adsorbed mass with the pseudo-first-order model was between 430 and 480 mg/g, which is close to the experimental data, thereby confirming the suitability of this model to describe the adsorption phenomenon [67]. This result also suggests that the adsorption of MB and OG by the AgMOF, GO-AgMOF, and MXene-AgMOF follows physisorption.

The fitted experimental data with the intra-particle diffusion model describes two different stages for the adsorption of MB: First, adsorption starts with an initial sharp increase, which can be due to the quick interaction of MB with the surface of the adsorbents, and then, adsorption reaches equilibrium because most of the MBs were already captured. However, for OG, most of the experimental data follow a linear trend, which is consistent with the higher R-squared data generated. Such linearity of the data can be ascribed to the adsorption mechanism related to intraparticle diffusion [68].

Adsorption Isotherms. Experimental adsorption data from Fig. 2 were analyzed using Freundlich, Langmuir, and Temkin isotherms (see Fig. 6), and the estimated parameters are presented in Table 3. These data suggest that the prediction from the Temkin model is not satisfactory, but the Langmuir and Freundlich models fit best with the experimental isotherm data, as they offered higher R-squared values, close to 1. The Freundlich model supports multilayer adsorption, while the Langmuir model supports monolayer adsorption [7]. However, the predicted maximum adsorption capacity by the Langmuir model is far off the experimental data; therefore Freundlich model is the most suitable one to explain the adsorption process in the present work.

Adsorption Mechanism. It may be noted that all three AgMOF-based NCs adsorbed more than 98% of MB in 24 h at pH 7, whereas the largest adsorption was demonstrated for OG at pH 3, which did not exceed 20% removal. Both GO-AgMOF and MXene-AgMOF NCs adsorbed larger fractions (99.9% and 99%, respectively) of MB, even at the

Table 2
The adsorption kinetics analysis of MB and OG.

Adsorbent/Dye	Pseudo-First-Order			Pseudo-Second-Order			Intra-Particle		
	q_e	k_1	R^2	q_e	k_2	R^2	C	k_{id}	R^2
MB									
AgMOF	479.5	0.08	0.96	30.1	0.02	0.85	−50.0	96.7	0.92
GO-AgMOF	428.0	0.14	0.97	30.5	0.02	0.65	−3.2	91.3	0.92
MXene-AgMOF	452.7	0.10	0.96	30.2	0.02	0.79	−36.6	95.3	0.92
OG									
AgMOF	51.5	0.14	0.99	18.9	0.007	0.67	0.3	10.8	0.95
GO-AgMOF	71.3	0.06	0.97	16.6	0.005	0.91	−7.2	7.2	0.94
MXene-AgMOF	71.3	0.06	0.98	19.1	0.007	0.90	−4.7	13.8	0.93

$q_{e\ (mg/g)}$: adsorption capacity.
$k_{1(1/min)}$: rate constant of Pseudo First Order model.
R^2: R-squared value.
$k_{2\ (1/min)}$: rate constant of Pseudo Second Order model.
$C_{(mg/g)}$: intercept.
$k_{id\ (1/min)}$: rate constant of Temkin model.

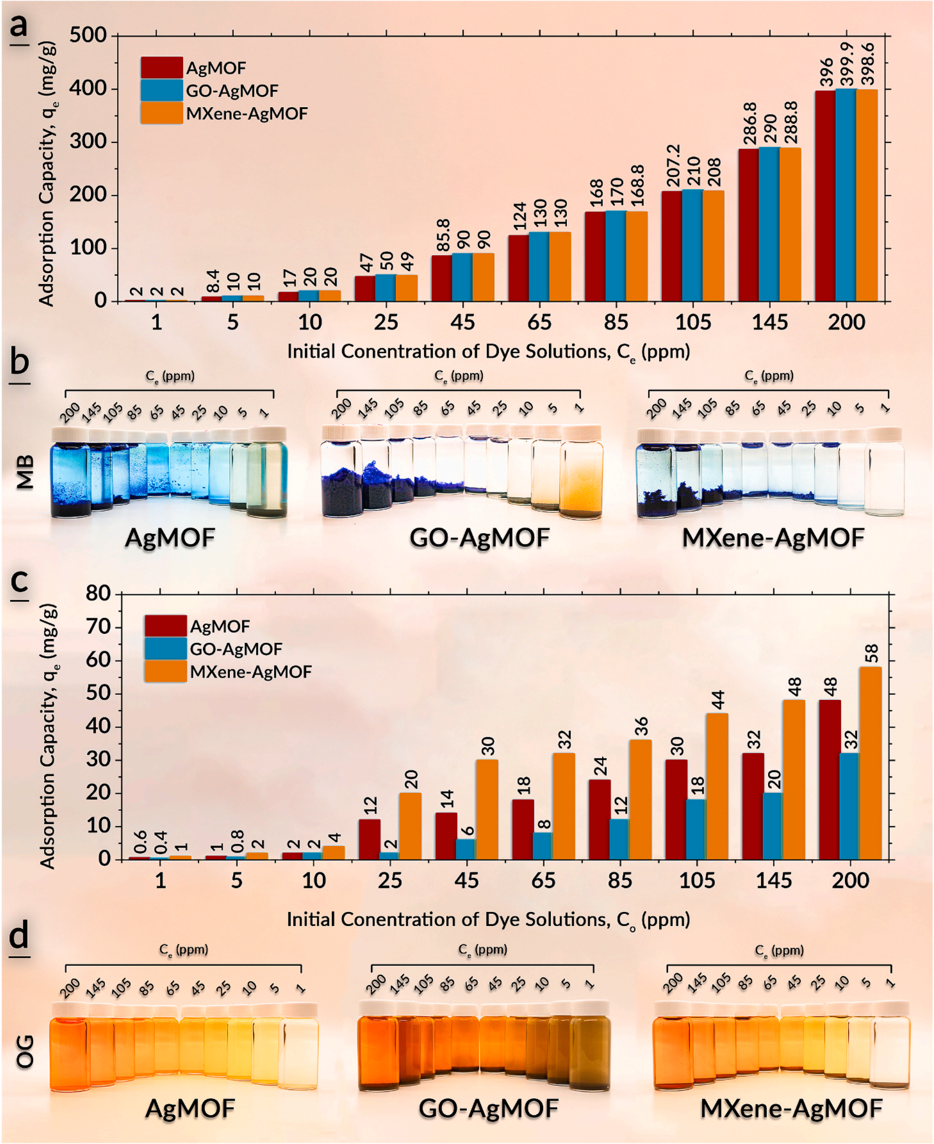

Fig. 3. The removal efficiency of AgMOF, GO-AgMOF, and MXene-AgMOF. The pH was set to 7 for all solutions at room temperature. **(a)** The removal efficiency of MB as a function of initial dye concentration in solution. **(b)** Photographs of the MB adsorption vials after 24 hours of the experiment. **(c)** The removal efficiency of OG as a function of initial dye concentration in solution. **(d)** Photographs of the OG adsorption vials after 24 hours of the experiment. All data in **(a)** and **(c)** are the average of three different experiments with a coefficient of variation lower than 10%.

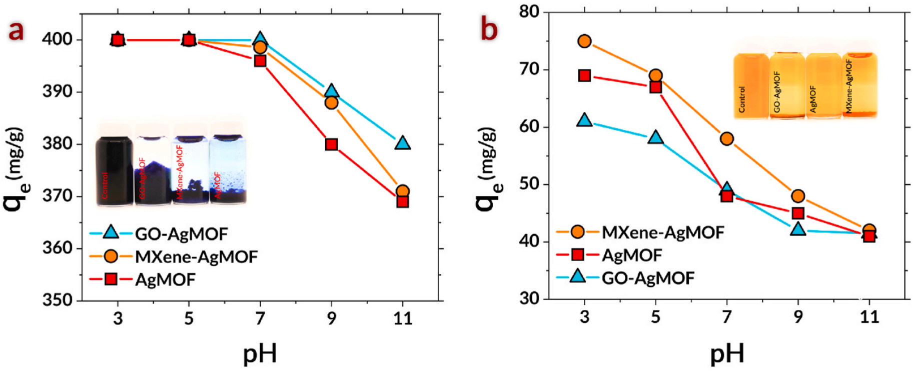

Fig. 4. Effect of pH on the removal efficiency of **(a)** MB and **(b)** OG. Photographs of the adsorption vials (at pH = 3) are shown within the graphs. The data points are the average of three different experiments with a coefficient of variation lower than 10%. Experiments were carried out at room temperature and the initial dye concentration was 200 mg/L.

high initial concentration of 200 mg/L. None of the NCs showed an acceptable adsorption efficiency towards OG. The adsorption kinetics analysis suggests that pseudo first order is the best predicting model for the adsorption of MB and OG by NCs since the model is based on physisorption rather than chemisorption [69]. In the case of physical adsorption, the zeta potential, surface area, and pore volume [7] are the

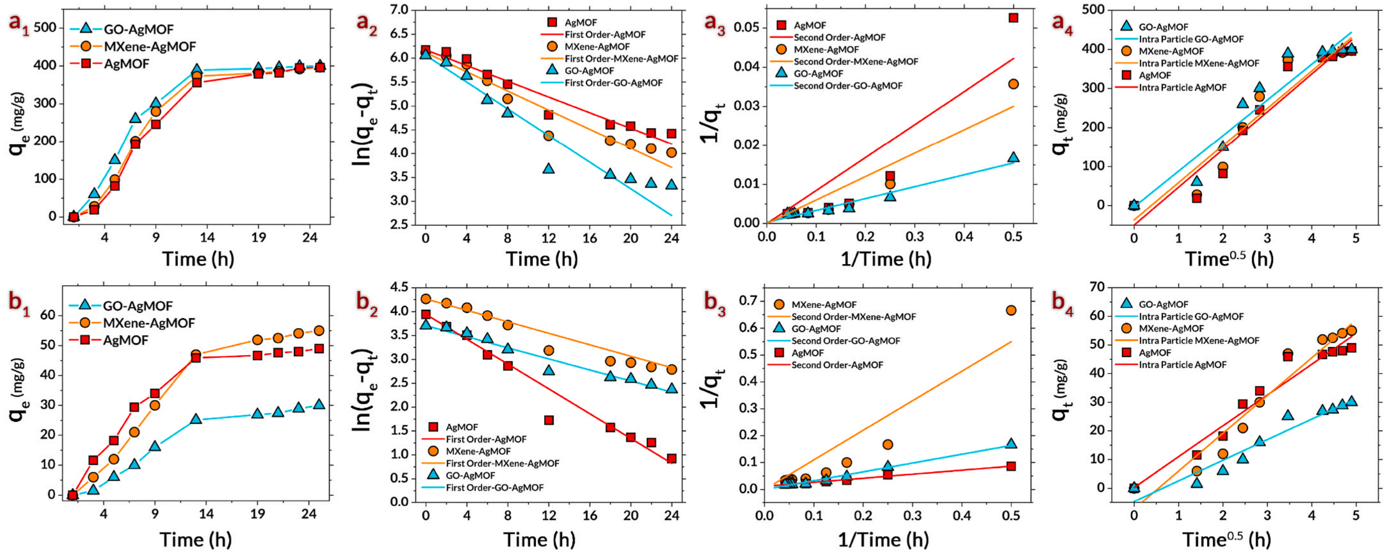

Fig. 5. The adsorption kinetics analysis of MB and OG. The initial concentration of dye solutions was 200 mg/L and experiments were carried out at pH 7 and room temperature. **(a_1)** The adsorption capacity of AgMOF, GO-AgMOF, and MXene-AgMOF versus time toward MB, **(a_2)** Pseudo-first-order model for adsorption of MB, **(a_3)** Pseudo-second-order model for adsorption of MB, **(a_4)** Intraparticle diffusion model for adsorption of MB, **(b_1)** The adsorption capacity of AgMOF, GO-AgMOF, and MXene-AgMOF versus time toward OG, **(b_2)** Pseudo-first-order model for adsorption of OG, **(b_3)** Pseudo-second-order model for adsorption of OG, **(b_4)** Intraparticle diffusion model for adsorption of OG. The pseudo-first-order model has the highest R-squared value for both dyes, describing the adsorption as physical adsorption. Here q_t stands for adsorption capacity at time t.

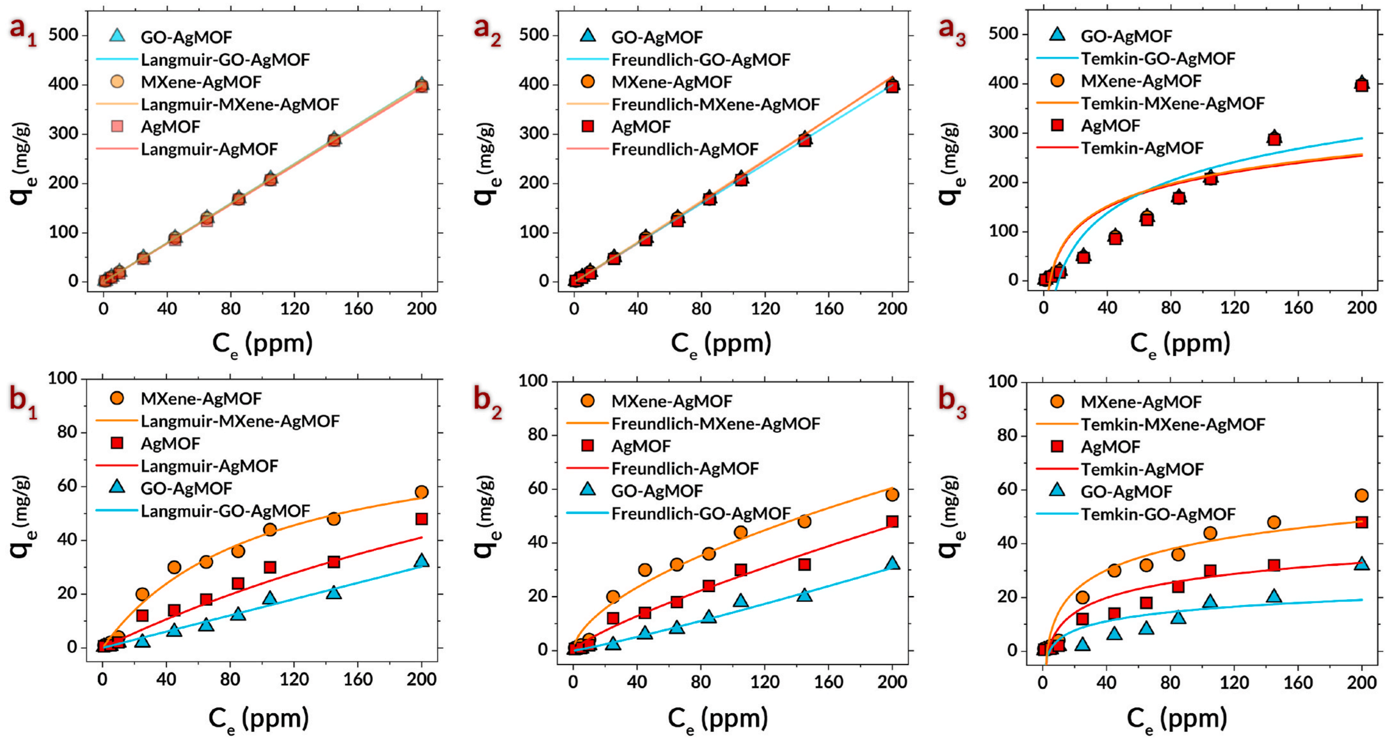

Fig. 6. The adsorption isotherm analysis of MB and OG. All experiments were carried out at room temperature and pH = 7. **(a_1)** Experimental data and Langmuir model prediction of AgMOF, GO-AgMOF, and MXene-AgMOF for MB, **(a_2)** Experimental data and Freundlich model prediction of AgMOF, GO-AgMOF, and MXene-AgMOF for MB, **(a_3)** Experimental data and Temkin model prediction of AgMOF, GO-AgMOF, and MXene-AgMOF for MB, **(b_1)** Experimental data and Langmuir model prediction of AgMOF, GO-AgMOF, and MXene-AgMOF for OG, **(b_2)** Experimental data and Freundlich model prediction of AgMOF, GO-AgMOF, and MXene-AgMOF for OG, **(b_3)** Experimental data and Temkin model prediction of AgMOF, GO-AgMOF, and MXene-AgMOF for OG. Freundlich's model best describes the adsorption behavior in which dye is captured in multilayers (as a result of physical adsorption).

main properties driving the mechanism of removal of dyes and contaminants from the solution because the first is related to the electrostatic driving force, while surface area and pore volume are associated with the availability of adsorption sites [54]. GO-AgMOF and MXene-AgMOF had higher surface area than AgMOF. MXene and GO are highly porous materials, and their incorporation into the AgMOF would increase the overall surface area and pore volume of the NCs [50,61]. GO-AgMOF has the highest negative surface charge, thus explaining its

Table 3
Adsorption isotherm analysis of MB and OG.

Adsorbent/Dye	Langmuir Model			Freundlich Model			Temkin Model		
	q_m(x10^3)	k_L	R^2	k_F	n	R^2	k_T	B	R^2
MB									
AgMOF	134.3	1.47	0.99	1.8	0.9	0.99	0.25	65.0	0.69
GO-AgMOF	87.9	2.28	0.99	2.0	1.0	1.0	0.11	94.0	0.79
MXene-AgMOF	72.7	2.75	0.99	1.9	0.9	0.99	0.25	65.3	0.69
OG									
AgMOF	0.14	0.002	0.99	0.67	1.25	0.98	0.30	8.11	0.77
GO-AgMOF	45.0	3.364	0.97	0.08	0.89	0.99	0.25	5.0	0.64
MXene-AgMOF	0.08	0.010	0.98	2.68	1.71	0.97	0.37	11.3	0.88

q_m (mg/g): maximum adsorption capacity.
k_L (l/mg): Langmuir equilibrium constant.
R^2: R-squared value.
k_F: Freundlich adsorption capacity constant.
n: adsorption intensity.
k_T (l/mg): Temkin equilibrium constant.
B: Temkin constant.

higher adsorption rates. In conclusion, the synergetic effect of more negative surface charge, larger surface area, and higher pore volume helped GO-AgMOF to excel in MB adsorption efficacy compared to AgMOF.

Adsorption Characteristics. To fully characterize the adsorption of the MB and OG on the NCs, XRD (Fig. 7a$_1$-a$_3$) and Raman spectroscopy (Fig. 7b$_1$-b$_3$) analyses were performed. Fig. 7a$_3$ presents the XRD spectra of MXene-AgMOF, MXene-AgMOF-MB (the MXene-AgMOF NCs after adsorption of MB), and MXene-AgMOF-OG (the MXene-AgMOF NCs after adsorption of OG). The peaks at around 17.05° and 27.34° can be attributed to the diffractions of (004) and (006) planes in MXene [70,71]. These peaks are substantially shifted for MXene-AgMOF-MB to lower angles at 16.8° and 27.13°. These shifts are more subtle for MXene-AgMOF-OG. Furthermore, the appearance of two new low-intensity peaks at 43.85° and 46.53° in the MXene-AgMOF-MB spectrum and their absence in MXene-AgMOF and MXene-AgMOF-OG spectra may be rationalized as higher adsorption rates of MB in MXene-AgMOF-MB [72,73]. XRD spectra of GO-AgMOF, GO-AgMOF-MB, and GO-AgMOF-OG are shown in Fig. 7a$_2$. Considering the GO-AgMOF spectrum, the characteristic peaks of GO are observed at 2θ = 10.15° and 24.72° [74,75]. The latter disappeared in loaded samples, and the former shifted with a different intensity [7,76]. Lastly, XRD spectra of AgMOF, AgMOF-MB, and AgMOF-OG are presented in Fig. 7a$_1$. The indicative peak of Ag (111) was observed at around 2θ = 36.49° [77,78]. The peaks at 6.15°, 10.85°, and 13.10° may respectively be ascribed to (110), (200), and (211) diffraction indices of AgMOF [78,79]. Overall, the spectra for loaded samples followed the same pattern as pristine samples but with considerable peak shifts. The corresponding peaks of (110), (200), and (211) indices were respectively shifted to 6.29°, 10.97°, and 13.25° for the loaded samples. Besides, Ag (111) shifted to 36.59°.

The Raman spectra of GO-AgMOF and loaded GO-AgMOF-MB and GO-AgMOF-OG are presented in Fig. 7b$_2$. A typical Raman spectrum of GO is characterized by two high-intensity peaks, referred to as the G band at ~1597 cm^{-1}, corresponding to CC bonding, and the D band at ~1353 cm^{-1} [80–82]. Here, the corresponding G band and D band of the GO-AgMOF sample were respectively observed at ~1569 cm^{-1} and ~1528 cm^{-1}, slightly red-shifted due to disorders and/or defects caused by bonding with AgMOF ligand and Ag ions [83,84]. This shift was slightly more pronounced for the Raman spectrum of GO-AgMOF-MB, for which the assigned peak of the G band was detected at ~1559 cm^{-1}. This further shift, in addition to the intensity change, suggests that the adsorption process was related to the bondage between active groups of GO-AgMOF and MB. However, the shift was smaller in the Raman spectrum of GO-AgMOF-OG (blue-shifted compared to GO-AgMOF spectrum), showing the assigned G band at ~1584 cm^{-1} with a much lower intensity, supporting some adsorption of OG but not as much as MB.

Fig. 7b$_3$ shows the Raman spectra of MXene-AgMOF, MXene-AgMOF-MB, and MXene-AgMOF-OG samples. Again, the two dominant

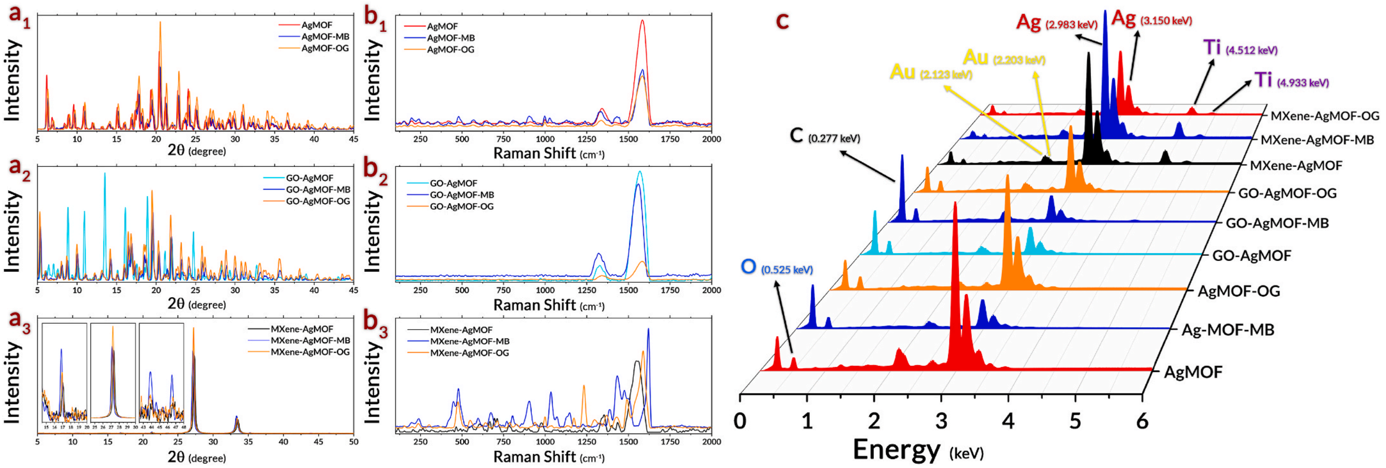

Fig. 7. **(a$_1$-a$_3$)** XRD analysis of NCs before and after the adsorption, **(b$_1$-b$_3$)** Raman spectroscopy of the NCs before and after the adsorption, and **(c)** EDS spectrum of the NCs before and after the adsorption.

peaks at ~1553 and ~1349 cm^{-1} are attributed to the aromatic benzene ring in the AgMOF ligand. Indicative bands of $Ti_3C_2T_x$ MXene are reported to be at 210, 630, and 730 cm^{-1} [85,86]. These peaks were actually detected approximately at 205, 620, and 711 cm^{-1}, slightly shifted, most probably due to the interaction with the AgMOF ligand. The Raman peaks at 205 and 711 cm^{-1} are respectively associated with the Ti–C and C–C vibrations of our oxygen-terminated MXene $Ti_3C_2T_x$, known as A_{1g} symmetry vibrations [87]. The peak at 620 cm^{-1} is mainly caused by C atoms vibrations (known as E_g vibrations) in the OH-terminated MXene [58] which has not been used in the experiment. This peak is still detected because the interaction of MXene with AgMOF ligands could replace one oxygen atom with a hydrogen atom, turning some oxygen-terminated MXene into an OH-terminated MXene structure. In the Raman spectrum of the MXene-AgMOF-MB sample, the characteristic peaks of MB at 447, 769, 1147, 1387, and 1620 cm^{-1} [88] were observed with slight shifts because of the bond-forming with the adsorbents. The peak at 447 cm^{-1} is assigned to the C–N–C deformation mode [89]. Peaks at 769 and 1147 cm^{-1} are due to C–H in-plane bending modes [89]. C–N symmetrical stretching mode is observed at 1387 cm^{-1} [90,91]. The dominant peak at 1620 is corresponded to the C–C ring stretching [89,92]. Noticeably, this peak is asymmetric with a shoulder at lower energy, caused mainly by the aromatic ring in the AgMOF ligand. It should be mentioned that the peak associated with the Ti–C vibrations is still observed in the spectrum with a slight shift at ~196 cm^{-1}. However, the peak associated with the C–C vibration of $Ti_3C_2T_x$ is absent or dominated by the peak at 769 cm^{-1}. Overall, the presence of MB indicative peaks and the adsorbents in the spectrum advocate that effective interaction occurs between them. The corresponding aromatic ring peak in the Raman spectrum of the MXene-AgMOF-OG sample is centered at 1589 and ~1369 cm^{-1}. The peaks at ~547 and ~1233 cm^{-1} are believed to be due to O–S–O and SO_3 vibrations [93,94] present in the OG structure. The peaks associated with the Ti–C and C–C vibrations of $Ti_3C_2T_x$ were also detected at ~199 and ~711 cm^{-1}. However, the intensity of these peaks was very low, suggesting the marginal adsorption of OG. For AgMOF (Fig. 7b$_1$), the strongest peak is localized at 1585 cm^{-1} and is recurrent in all three spectra. Moreover, the peak at ~996 cm^{-1} is most probably attributable to vibrations of silver atom bonding [95,96]. The second sharp peak is observed at 1343 cm^{-1} for the AgMOF spectrum, slightly shifted for AgMOF-MB (1333 cm^{-1}) and AgMOF-OG (1328 cm^{-1}) spectra. These shifts are due to the subtle change in the structure of AgMOF after interaction with dyes, suggesting the adsorption has been successfully implemented, especially for MB.

The energy dispersive spectroscopy (EDS) spectra of the NCs, before and after the adsorption, are displayed in Fig. 7c. Also, the mapping images of all critical elements are reported in Figs. S2–S10. In summary, the characteristic peaks of titanium for MXene-AgMOF and silver for all materials were detected in the EDS spectra, while sulfur as an element that exists in both MB and OG was mapped for all the materials after adsorption (Figs. S2–S10) confirming the capture of both dyes.

4. Conclusion

In this work, GO and MXene sheets were combined with AgMOF to obtain NCs of GO-AgMOF and MXene-AgMOF and to investigate their adsorption properties toward MB and OG. All NCs were fully characterized using SEM, TEM, XRD, and Raman spectroscopy. All three NCs adsorbed more than 98% of MB in 24 h, whereas the largest adsorption was demonstrated for OG (at pH 3), but which did not exceed 20% removal efficiency. GO-AgMOF and MXene-AgMOF NCs adsorbed more MB dye (99.9% and 99%, respectively, even at a high initial dye concentration of 200 mg/L) compared to AgMOF. However, none of the NCs showed acceptable adsorption efficiency towards OG. The batch adsorption tests confirmed the pseudo-first-order kinetic, supporting physisorption and electrostatic interaction as the main driving force. The results suggest that all three NCs can be promising adsorbents for MB, especially GO-AgMOF. Also, the composition of MXene with AgMOF followed a facile approach to enable the enhanced functionality of AgMOF, suggesting that MXene-AgMOF is a promising candidate for environmental remediation applications.

Declaration of competing interest

The authors declare that they have no known competing financial interests or personal relationships that could have appeared to influence the work reported in this paper.

Data availability

Data will be made available on request.

Acknowledgment

This research benefitted greatly from funding provided by USDA TAT-RWTS 00-69526. This paper has not been formally reviewed by USDA and the views expressed in this document are solely those of the authors and do not necessarily reflect those of USDA. USDA does not endorse any products or commercial services mentioned in this publication. USDA had no role in the study design, data collection, analysis, decision to publish, or preparation of the manuscript. Also, the authors are expressing their gratitude to Dr. Tejraj M. Aminabhavi for his time in editing the manuscript.

Appendix A. Supplementary data

Supplementary data to this article can be found online at https://doi.org/10.1016/j.cscee.2023.100296.

References

[1] H. Wang, H. Wang, Q. Yan, Peroxymonosulfate activation by algal carbocatalyst for organic dye oxidation: insights into experimental and theoretical, Sci. Total Environ. 816 (2022), 151611.

[2] S.M. Nejad, S.F. Seyedpour, S.A. Aktij, M.D. Firouzjaei, M. Elliott, A. Tiraferri, M. Sadrzadeh, A. Rahimpour, Loose nanofiltration membranes functionalized with in situ-synthesized metal organic framework for water treatment, Mater. Today Chem. 24 (2022), 100909.

[3] A. Aghaei, M.D. Firouzjaei, P. Karami, S.A. Aktij, M. Elliott, Y. Mansourpanah, A. Rahimpour, J.B.P. Soares, M. Sadrzadeh, The implications of 3D-printed membranes for water and wastewater treatment and resource recovery, Can. J. Chem. Eng. 100 (2022) 2309–2321, https://doi.org/10.1002/cjce.24488.

[4] J.-F. Ma, Y.-N. Hou, J. Guo, H.M.A. Sharif, C. Huang, J. Zhao, H. Li, Y. Song, C. Lu, Y. Han, Rational design of biogenic PdxAuy nanoparticles with enhanced catalytic performance for electrocatalysis and azo dyes degradation, Environ. Res. 204 (2022), 112086.

[5] A. Singh, D.B. Pal, A. Mohammad, A. Alhazmi, S. Haque, T. Yoon, N. Srivastava, V. K. Gupta, Biological remediation technologies for dyes and heavy metals in wastewater treatment: new insight, Bioresour. Technol. 343 (2022), 126154.

[6] L. Wolski, K. Sobańska, A. Walkowiak, K. Akhmetova, J. Gryboś, M. Frankowski, M. Ziolek, P. Pietrzyk, Enhanced adsorption and degradation of methylene blue over mixed niobium-cerium oxide–Unraveling the synergy between Nb and Ce in advanced oxidation processes, J. Hazard Mater. 415 (2021), 125665.

[7] M.D. Firouzjaei, F.A. Afkhami, M.R. Esfahani, C.H. Turner, S. Nejati, Experimental and molecular dynamics study on dye removal from water by a graphene oxide-copper-metal organic framework nanocomposite, J. Water Proc. Eng. 34 (2020), 101180.

[8] N. Mohammed, H. Lian, M.S. Islam, M. Strong, Z. Shi, R.M. Berry, H.-Y. Yu, K. C. Tam, Selective adsorption and separation of organic dyes using functionalized cellulose nanocrystals, Chem. Eng. J. 417 (2021), 129237, https://doi.org/10.1016/j.cej.2021.129237.

[9] M. Dadashi Firouzjaei, E. Zolghadr, S. Ahmadalipour, N. Taghvaei, F. Akbari Afkhami, S. Nejati, M.A. Elliott, Chemistry, abundance, detection and treatment of per- and polyfluoroalkyl substances in water: a review, Environ. Chem. Lett. 20 (2022) 661–679, https://doi.org/10.1007/s10311-021-01340-6.

[10] E. Zolghadr, M.D. Firouzjaei, G. Amouzandeh, P. LeClair, M. Elliott, The role of membrane-based technologies in environmental treatment and reuse of produced water, Front. Environ. Sci. (2021) 71.

[11] M.D. Firouzjaei, S.F. Seyedpour, S.A. Aktij, M. Giagnorio, N. Bazrafshan, A. Mollahosseini, F. Samadi, S. Ahmadalipour, F.D. Firouzjaei, M.R. Esfahani, A. Tiraferri, M. Elliott, M. Sangermano, A. Abdelrasoul, J.R. McCutcheon, M. Sadrzadeh, A.R. Esfahani, A. Rahimpour, Recent advances in functionalized polymer membranes for biofouling control and mitigation in forward osmosis,

J. Membr. Sci. 596 (2020), 117604, https://doi.org/10.1016/j.memsci.2019.117604.

[12] C. Zhao, B. Wang, B.K.G. Theng, P. Wu, F. Liu, S. Wang, X. Lee, M. Chen, L. Li, X. Zhang, Formation and mechanisms of nano-metal oxide-biochar composites for pollutants removal: a review, Sci. Total Environ. 767 (2021), 145305.

[13] H. Xue, X. Gao, M.K. Seliem, M. Mobarak, R. Dong, X. Wang, K. Fu, Q. Li, Z. Li, Efficient adsorption of anionic azo dyes on porous heterostructured MXene/biomass activated carbon composites: experiments, characterization, and theoretical analysis via advanced statistical physics models, Chem. Eng. J. 451 (2023), 138735.

[14] I.O. Saheed, W. da Oh, F.B.M. Suah, Chitosan modifications for adsorption of pollutants–A review, J. Hazard Mater. 408 (2021), 124889.

[15] A. Yadav, S.S. Dindorkar, S.B. Ramisetti, N. Sinha, Simultaneous adsorption of methylene blue and arsenic on graphene, boron nitride and boron carbon nitride nanosheets: insights from molecular simulations, J. Water Proc. Eng. 46 (2022), 102653.

[16] J.-Y. Cheng, P. Wang, J.-P. Ma, Q.-K. Liu, Y.-B. Dong, A nanoporous Ag(i)-MOF showing unique selective adsorption of benzene among its organic analogues, Chem. Commun. 50 (2014) 13672–13675, https://doi.org/10.1039/C4CC03204G.

[17] A.M. Omer, E.M. Abd El-Monaem, G.M. El-Subruiti, M.M. Abd El-Latif, A. S. Eltaweil, Fabrication of easy separable and reusable MIL-125(Ti)/MIL-53(Fe) binary MOF/CNT/Alginate composite microbeads for tetracycline removal from water bodies, Sci. Rep. 11 (2021), 23818, https://doi.org/10.1038/s41598-021-03428-z.

[18] A. Zirehpour, A. Rahimpour, S. Khoshhal, M.D. Firouzjaei, A.A. Ghoreyshi, The impact of MOF feasibility to improve the desalination performance and antifouling properties of FO membranes, RSC Adv. 6 (2016) 70174–70185, https://doi.org/10.1039/C6RA14591D.

[19] S.F. Seyedpour, A. Arabi Shamsabadi, S. Khoshhal Salestan, M. Dadashi Firouzjaei, M. Sharifian Gh, A. Rahimpour, F. Akbari Afkhami, M. reza Shirzad Kebria, M. A. Elliott, A. Tiraferri, Tailoring the biocidal activity of novel silver-based metal azolate frameworks, ACS Sustain. Chem. Eng. 8 (2020) 7588–7599.

[20] N. Bazrafshan, M. Dadashi Firouzjaei, M. Elliott, A. Moradkhani, A. Rahimpour, Preparation and modification of low-fouling ultrafiltration membranes for cheese whey treatment by membrane bioreactor, Case Stud. Chem. Environ. Eng. 4 (2021), 100137, https://doi.org/10.1016/j.cscee.2021.100137.

[21] S.F. Seyedpour, M. Dadashi Firouzjaei, A. Rahimpour, E. Zolghadr, A. Arabi Shamsabadi, P. Das, F. Akbari Afkhami, M. Sadrzadeh, A. Tiraferri, M. Elliott, Toward sustainable tackling of biofouling implications and improved performance of TFC FO membranes modified by Ag-MOF nanorods, ACS Appl. Mater. Interfaces 12 (2020) 38285–38298, https://doi.org/10.1021/acsami.0c13029.

[22] E. Zolghadr, M. Dadashi Firouzjaei, S. Aghapour Aktij, A. Aghaei, E.K. Wujcik, M. Sadrzadeh, A. Rahimpour, F.A. Afkhami, P. LeClair, M. Elliott, An ultrasonic-assisted rapid approach for sustainable fabrication of antibacterial and anti-biofouling membranes via metal-organic frameworks, Mater. Today Chem. 26 (2022), 101044, https://doi.org/10.1016/j.mtchem.2022.101044.

[23] M. Mozafari, S.F. Seyedpour, S.K. Salestan, A. Rahimpour, A.A. Shamsabadi, M. D. Firouzjaei, M.R. Esfahani, A. Tiraferri, H. Mohsenian, M. Sangermano, M. Soroush, Facile Cu-BTC surface modification of thin chitosan film coated polyethersulfone membranes with improved antifouling properties for sustainable removal of manganese, J. Membr. Sci. 588 (2019), 117200, https://doi.org/10.1016/j.memsci.2019.117200.

[24] M.R.S. Kebria, A. Rahimpour, G. Bakeri, R. Abedini, Experimental and theoretical investigation of thin ZIF-8/chitosan coated layer on air gap membrane distillation performance of PVDF membrane, Desalination 450 (2019) 21–32, https://doi.org/10.1016/j.desal.2018.10.023.

[25] M. Dadashi Firouzjaei, M. Pejman, M.S. Gh, S.A. Aktij, E. Zolghadr, A. Rahimpour, M. Sadrzadeh, A.A. Shamsabadi, A. Tiraferri, M. Elliott, Functionalized polyamide membranes yield suppression of biofilm and planktonic bacteria while retaining flux and selectivity, Separ. Purif. Technol. 282 (2022), 119981, https://doi.org/10.1016/j.seppur.2021.119981.

[26] M. Pejman, M.D. Firouzjaei, S.A. Aktij, P. Das, E. Zolghadr, H. Jafarian, A. A. Shamsabadi, M. Elliott, M.R. Esfahani, M. Sangermano, M. Sadrzadeh, E. K. Wujcik, A. Rahimpour, A. Tiraferri, Improved antifouling and antibacterial properties of forward osmosis membranes through surface modification with zwitterions and silver-based metal organic frameworks, J. Membr. Sci. 611 (2020), 118352, https://doi.org/10.1016/j.memsci.2020.118352.

[27] M. Pejman, M. Dadashi Firouzjaei, S. Aghapour Aktij, P. Das, E. Zolghadr, H. Jafarian, A. Arabi Shamsabadi, M. Elliott, M. Sadrzadeh, M. Sangermano, A. Rahimpour, A. Tiraferri, In situ Ag-MOF growth on pre-grafted zwitterions imparts outstanding antifouling properties to forward osmosis membranes, ACS Appl. Mater. Interfaces 12 (2020) 36287–36300, https://doi.org/10.1021/acsami.0c12141.

[28] Q.-L. Zhu, Q. Xu, Metal–organic framework composites, Chem. Soc. Rev. 43 (2014) 5468–5512.

[29] M. Berchel, T. Le Gall, C. Denis, S. Le Hir, F. Quentel, C. Elléouet, T. Montier, J.-M. Rueff, J.-Y. Salaün, J.-P. Haelters, A silver-based metal–organic framework material as a 'reservoir'of bactericidal metal ions, New J. Chem. 35 (2011) 1000–1003.

[30] M. Pejman, M. Dadashi Firouzjaei, S. Aghapour Aktij, E. Zolghadr, P. Das, M. Elliott, M. Sadrzadeh, M. Sangermano, A. Rahimpour, A. Tiraferri, Effective strategy for UV-mediated grafting of biocidal Ag-MOFs on polymeric membranes aimed at enhanced water ultrafiltration, Chem. Eng. J. 426 (2021), 130704, https://doi.org/10.1016/j.cej.2021.130704.

[31] G. Zhan, H.C. Zeng, Alternative synthetic approaches for metal–organic frameworks: transformation from solid matters, Chem. Commun. 53 (2017) 72–81.

[32] H.S. Far, M. Hasanzadeh, M.S. Nashtaei, M. Rabbani, A. Haji, B. Hadavi Moghadam, PPI-Dendrimer-Functionalized magnetic metal–organic framework (Fe3O4@ MOF@ PPI) with high adsorption capacity for sustainable wastewater treatment, ACS Appl. Mater. Interfaces 12 (2020) 25294–25303.

[33] S.A. Qamar, M. Ashiq, M. Jahangeer, A. Riasat, M. Bilal, Chitosan-based hybrid materials as adsorbents for textile dyes–A review, Case Stud. Chem. Environ. Eng. 2 (2020), 100021.

[34] M. Daud, A. Hai, F. Banat, M.B. Wazir, M. Habib, G. Bharath, M.A. Al-Harthi, A review on the recent advances, challenges and future aspect of layered double hydroxides (LDH)–Containing hybrids as promising adsorbents for dyes removal, J. Mol. Liq. 288 (2019), 110989.

[35] I. Khurana, A. Saxena, J.M. Khurana, P.K. Rai, Removal of dyes using graphene-based composites: a review, Water Air Soil Pollut. 228 (2017) 1–17.

[36] S.K. Fanourakis, J. Peña-Bahamonde, P.C. Bandara, D.F. Rodrigues, Nano-based adsorbent and photocatalyst use for pharmaceutical contaminant removal during indirect potable water reuse, NPJ Clean Water 3 (2020) 1, https://doi.org/10.1038/s41545-019-0048-8.

[37] E.M. Abd El-Monaem, A.M. Omer, R.E. Khalifa, A.S. Eltaweil, Floatable cellulose acetate beads embedded with flower-like zwitterionic binary MOF/PDA for efficient removal of tetracycline, J. Colloid Interface Sci. 620 (2022) 333–345, https://doi.org/10.1016/j.jcis.2022.04.010.

[38] Z. Geng, Y. Lin, X. Yu, Q. Shen, L. Ma, Z. Li, N. Pan, X. Wang, Highly efficient dye adsorption and removal: a functional hybrid of reduced graphene oxide–Fe 3 O 4 nanoparticles as an easily regenerative adsorbent, J. Mater. Chem. 22 (2012) 3527–3535.

[39] C. Liu, H. Liu, K. Zhang, M. Dou, B. Pan, X. He, C. Lu, Partly reduced graphene oxide aerogels induced by proanthocyanidins for efficient dye removal, Bioresour. Technol. 282 (2019) 148–155.

[40] A. VahidMohammadi, J. Rosen, Y. Gogotsi, The world of two-dimensional carbides and nitrides (MXenes), Science 372 (2021), eabf1581.

[41] A.A. Shamsabadi, A.P. Isfahani, S.K. Salestan, A. Rahimpour, B. Ghalei, E. Sivaniah, M. Soroush, Pushing rubbery polymer membranes to Be economic for CO2 separation: embedment with Ti3C2Tx MXene nanosheets, ACS Appl. Mater. Interfaces 12 (2020) 3984–3992, https://doi.org/10.1021/acsami.9b19960.

[42] B. Anasori, M.R. Lukatskaya, Y. Gogotsi, 2D metal carbides and nitrides (MXenes) for energy storage, Nat. Rev. Mater. 2 (2017) 1–17.

[43] B. Anasori, Û.G. Gogotsi, 2D Metal Carbides and Nitrides (MXenes), Springer, 2019.

[44] M. Dadashi Firouzjaei, M. Karimiziarani, H. Moradkhani, M. Elliott, B. Anasori, MXenes: the two-dimensional influencers, Mater. Today Adv. 13 (2022), 100202, https://doi.org/10.1016/j.mtadv.2021.100202.

[45] H. Jafarian, M. Dadashi Firouzjaei, S. Aghapour Aktij, A. Aghaei, M. Pilevar Khomami, M. Elliott, E.K. Wujcik, M. Sadrzadeh, A. Rahimpour, Synthesis of heterogeneous metal organic Framework-Graphene oxide nanocomposite membranes for water treatment, Chem. Eng. J. 455 (2023), 140851, https://doi.org/10.1016/j.cej.2022.140851.

[46] Y. Rezaeipour, E. Zolghadr, P. Alizadeh, G. Sadri, E.K. Wujcik, F.A. Afkhami, M. Elliott, M. Dadashi Firouzjaei, The anticancer properties of metal-organic frameworks and their heterogeneous nanocomposites, Biomater. Adv. 139 (2022), 213013, https://doi.org/10.1016/j.bioadv.2022.213013.

[47] I.K. Basha, E.M. Abd El-Monaem, R.E. Khalifa, A.M. Omer, A.S. Eltaweil, Sulfonated graphene oxide impregnated cellulose acetate floated beads for adsorption of methylene blue dye: optimization using response surface methodology, Sci. Rep. 12 (2022) 9339, https://doi.org/10.1038/s41598-022-13105-4.

[48] A.A. Shamsabadi, M.S. Gh, B. Anasori, M. Soroush, Antimicrobial mode-of-action of colloidal Ti3C2TX MXene nanosheets, ACS Sustain. Chem. Eng. 6 (2018) 16586–16596.

[49] P. Karami, S.A. Aktij, B. Khorshidi, M.D. Firouzjaei, A. Asad, M. Elliott, A. Rahimpour, J.B.P. Soares, M. Sadrzadeh, Nanodiamond-decorated thin film composite membranes with antifouling and antibacterial properties, Desalination 522 (2022), 115436, https://doi.org/10.1016/j.desal.2021.115436.

[50] M.D. Firouzjaei, A.A. Shamsabadi, M.S. Gh, A. Rahimpour, M. Soroush, A novel nanocomposite with superior antibacterial activity: a silver-based metal organic framework embellished with graphene oxide, Adv. Mater. Interfac. 5 (2018) 1701365.

[51] A. Patri, T. Umbreit, J. Zheng, K. Nagashima, P. Goering, S. Francke-Carroll, E. Gordon, J. Weaver, T. Miller, N. Sadrieh, Energy dispersive X-ray analysis of titanium dioxide nanoparticle distribution after intravenous and subcutaneous injection in mice, J. Appl. Toxicol.: Int. J. 29 (2009) 662–672.

[52] A. Patri, T. Umbreit, J. Zheng, K. Nagashima, P. Goering, S. Francke-Carroll, E. Gordon, J. Weaver, T. Miller, N. Sadrieh, Energy dispersive X-ray analysis of titanium dioxide nanoparticle distribution after intravenous and subcutaneous injection in mice, J. Appl. Toxicol.: Int. J. 29 (2009) 662–672.

[53] S. Kalathil, J. Lee, M.H. Cho, Electrochemically active biofilm-mediated synthesis of silver nanoparticles in water, Green Chem. 13 (2011) 1482–1485.

[54] Y. Dong, D. Sang, C. He, X. Sheng, L. Lei, Mxene/alginate composites for lead and copper ion removal from aqueous solutions, RSC Adv. 9 (2019) 29015–29022.

[55] E. Satheeshkumar, T. Makaryan, A. Melikyan, H. Minassian, Y. Gogotsi, M. Yoshimura, One-step solution processing of Ag, Au and Pd@ MXene hybrids for SERS, Sci. Rep. 6 (2016) 1–9.

[56] T. Hu, J. Wang, H. Zhang, Z. Li, M. Hu, X. Wang, Vibrational properties of Ti 3 C 2 and Ti 3 C 2 T 2 (T= O, F, OH) monosheets by first-principles calculations: a comparative study, Phys. Chem. Chem. Phys. 17 (2015) 9997–10003.

[57] O.E. Kaipoldayev, A.D. Muradov, Y.S. Mukhametkarimov, R.R. Nemkayeva, G. A. Baigarinova, M.B. Aitzhanov, N.R. Guseinov, Titanium Carbide Obtained by Magnetron Sputtering of Graphite on Heated Titanium Substrate, 2017.
[58] A. Sarycheva, T. Makaryan, K. Maleski, E. Satheeshkumar, A. Melikyan, H. Minassian, M. Yoshimura, Y. Gogotsi, Two-dimensional titanium carbide (MXene) as surface-enhanced Raman scattering substrate, J. Phys. Chem. C 121 (2017) 19983–19988.
[59] M. Alhabeb, K. Maleski, B. Anasori, P. Lelyukh, L. Clark, S. Sin, Y. Gogotsi, Guidelines for synthesis and processing of two-dimensional titanium carbide (Ti3C2T x MXene), Chem. Mater. 29 (2017) 7633–7644.
[60] L. Zhang, W. Su, Y. Huang, H. Li, L. Fu, K. Song, X. Huang, J. Yu, C.-T. Lin, In situ high-pressure X-ray diffraction and Raman spectroscopy study of Ti 3 C 2 T x MXene, Nanoscale Res. Lett. 13 (2018) 1–8.
[61] Y. Gogotsi, B. Anasori, The Rise of MXenes, 2019.
[62] M.D. Firouzjaei, A.A. Shamsabadi, S.A. Aktij, S.F. Seyedpour, M. Sharifian Gh, A. Rahimpour, M.R. Esfahani, M. Ulbricht, M. Soroush, Exploiting synergetic effects of graphene oxide and a silver-based metal–organic framework to enhance antifouling and anti-biofouling properties of thin-film nanocomposite membranes, ACS Appl. Mater. Interfaces 10 (2018) 42967–42978.
[63] M. Skoczylas, S. Bocian, B. Buszewski, Influence of silica functionalization by amino acids and peptides on the stationary phases zeta potential, J. Chromatogr. A 1573 (2018) 98–106.
[64] G. Fagerlund, Determination of specific surface by the BET method, Matériaux et Construct. 6 (1973) 239–245.
[65] D. Dollimore, G.R. Heal, Pore-size distribution in typical adsorbent systems, J. Colloid Interface Sci. 33 (1970) 508–519.
[66] A. Gürses, Ç. Doğar, M. Yalçın, M. Açıkyıldız, R. Bayrak, S. Karaca, The adsorption kinetics of the cationic dye, methylene blue, onto clay, J. Hazard Mater. 131 (2006) 217–228.
[67] W. Rudzinski, W. Plazinski, Studies of the kinetics of solute adsorption at solid/solution interfaces: on the possibility of distinguishing between the diffusional and the surface reaction kinetic models by studying the pseudo-first-order kinetics, J. Phys. Chem. C 111 (2007) 15100–15110.
[68] F.-C. Wu, R.-L. Tseng, R.-S. Juang, Initial behavior of intraparticle diffusion model used in the description of adsorption kinetics, Chem. Eng. J. 153 (2009) 1–8.
[69] Y.C. Wong, Y.S. Szeto, W.H. Cheung, G. McKay, Pseudo-first-order kinetic studies of the sorption of acid dyes onto chitosan, J. Appl. Polym. Sci. 92 (2004) 1633–1645.
[70] M. Alhabeb, K. Maleski, B. Anasori, P. Lelyukh, L. Clark, S. Sin, Y. Gogotsi, Guidelines for synthesis and processing of two-dimensional titanium carbide (Ti3C2T x MXene), Chem. Mater. 29 (2017) 7633–7644.
[71] L. Zhang, W. Su, Y. Huang, H. Li, L. Fu, K. Song, X. Huang, J. Yu, C.-T. Lin, In situ high-pressure X-ray diffraction and Raman spectroscopy study of Ti 3 C 2 T x MXene, Nanoscale Res. Lett. 13 (2018) 1–8.
[72] Y. Zhang, W. Wang, J. Zhang, P. Liu, A. Wang, A comparative study about adsorption of natural palygorskite for methylene blue, Chem. Eng. J. 262 (2015) 390–398.
[73] K. Ramesh, A. Rajappa, V. Nandhakumar, IR, XRD and SEM studies on the adsorption of methylene blue dye onto microwave assisted ZnCl2 activated carbon prepared from Delonix regia pods, Int. J. Curr. Res. Chem. Pharma. Sci. 1 (2014) 15–19.
[74] S.P. Deshmukh, D.P. Kale, S. Kar, S.R. Shirsath, B.A. Bhanvase, V.K. Saharan, S. H. Sonawane, Ultrasound assisted preparation of rGO/TiO2 nanocomposite for effective photocatalytic degradation of methylene blue under sunlight, Nano-Struct. Nano-Objects 21 (2020), 100407.
[75] M. Rafi, B. Samiey, C.-H. Cheng, Study of adsorption mechanism of Congo red on graphene oxide/PAMAM nanocomposite, Materials 11 (2018) 496.
[76] N.A. Travlou, G.Z. Kyzas, N.K. Lazaridis, E.A. Deliyanni, Functionalization of graphite oxide with magnetic chitosan for the preparation of a nanocomposite dye adsorbent, Langmuir 29 (2013) 1657–1668.
[77] H. Guo, Y. Zhang, Z. Zheng, H. Lin, Y. Zhang, Facile one-pot fabrication of Ag@ MOF (Ag) nanocomposites for highly selective detection of 2, 4, 6-trinitrophenol in aqueous phase, Talanta 170 (2017) 146–151.
[78] J. Liu, D.M. Strachan, P.K. Thallapally, Enhanced noble gas adsorption in Ag@ MOF-74Ni, Chem. Commun. 50 (2014) 466–468.
[79] R.L. Papurello, J.L. Fernández, E.E. Miró, J.M. Zamaro, Microreactor with silver-loaded metal-organic framework films for gas-phase reactions, Chem. Eng. J. 313 (2017) 1468–1476.
[80] A.Y. Lee, K. Yang, N.D. Anh, C. Park, S.M. Lee, T.G. Lee, M.S. Jeong, Raman study of D* band in graphene oxide and its correlation with reduction, Appl. Surf. Sci. 536 (2021), 147990.
[81] S.M. Hafiz, R. Ritikos, T.J. Whitcher, N.M. Razib, D.C.S. Bien, N. Chanlek, H. Nakajima, T. Saisopa, P. Songsiririthigul, N.M. Huang, A practical carbon dioxide gas sensor using room-temperature hydrogen plasma reduced graphene oxide, Sensor. Actuator. B Chem. 193 (2014) 692–700.
[82] F.T. Johra, J.-W. Lee, W.-G. Jung, Facile and safe graphene preparation on solution based platform, J. Ind. Eng. Chem. 20 (2014) 2883–2887.
[83] F. Tuinstra, J. Lo Koenig, Raman spectrum of graphite, J. Chem. Phys. 53 (1970) 1126–1130.
[84] F.T. Johra, J.-W. Lee, W.-G. Jung, Facile and safe graphene preparation on solution based platform, J. Ind. Eng. Chem. 20 (2014) 2883–2887.
[85] T. Hu, J. Wang, H. Zhang, Z. Li, M. Hu, X. Wang, Vibrational properties of Ti 3 C 2 and Ti 3 C 2 T 2 (T= O, F, OH) monosheets by first-principles calculations: a comparative study, Phys. Chem. Chem. Phys. 17 (2015) 9997–10003.
[86] O.E. Kaipoldayev, A.D. Muradov, Y.S. Mukhametkarimov, R.R. Nemkayeva, G. A. Baigarinova, M.B. Aitzhanov, N.R. Guseinov, Titanium Carbide Obtained by Magnetron Sputtering of Graphite on Heated Titanium Substrate, 2017.
[87] A. Sarycheva, T. Makaryan, K. Maleski, E. Satheeshkumar, A. Melikyan, H. Minassian, M. Yoshimura, Y. Gogotsi, Two-dimensional titanium carbide (MXene) as surface-enhanced Raman scattering substrate, J. Phys. Chem. C 121 (2017) 19983–19988.
[88] C. Li, Y. Huang, K. Lai, B.A. Rasco, Y. Fan, Analysis of trace methylene blue in fish muscles using ultra-sensitive surface-enhanced Raman spectroscopy, Food Control 65 (2016) 99–105.
[89] C. Li, Y. Huang, K. Lai, B.A. Rasco, Y. Fan, Analysis of trace methylene blue in fish muscles using ultra-sensitive surface-enhanced Raman spectroscopy, Food Control 65 (2016) 99–105.
[90] G.-N. Xiao, S.-Q. Man, Surface-enhanced Raman scattering of methylene blue adsorbed on cap-shaped silver nanoparticles, Chem. Phys. Lett. 447 (2007) 305–309.
[91] R.R. Naujok, R. V Duevel, R.M. Corn, Fluorescence and Fourier transform surface-enhanced Raman scattering measurements of methylene blue adsorbed onto a sulfur-modified gold electrode, Langmuir 9 (1993) 1771–1774.
[92] G.-N. Xiao, S.-Q. Man, Surface-enhanced Raman scattering of methylene blue adsorbed on cap-shaped silver nanoparticles, Chem. Phys. Lett. 447 (2007) 305–309.
[93] L. Zhang, W. Lian, P. Li, H. Ma, X. Han, B. Zhao, Z. Chen, Crocein Orange G mediated detection and modulation of amyloid fibrillation revealed by surface-enhanced Raman spectroscopy, Biosens. Bioelectron. 148 (2020), 111816.
[94] R.J. Gillespie, E.A. Robinson, Raman spectra of the H2SO4–SO3 and D2SO4–SO3 systems: evidence for the occurrence of polysulphuric acids, Can. J. Chem. 40 (1962) 658–674.
[95] J.-C. Valmalette, Z. Tan, H. Abe, S. Ohara, Raman scattering of linear chains of strongly coupled Ag nanoparticles on SWCNTs, Sci. Rep. 4 (2014) 1–8.
[96] Y. Meng, X. Yan, Y. Wang, A simple preparation of Ag@ graphene nanocomposites for surface-enhanced Raman spectroscopy of fluorescent anticancer drug, Chem. Phys. Lett. 651 (2016) 84–87.